Symmetrization of diffraction peak profiles measured with a high-resolution synchrotron X-ray powder diffractometer

T. Ida and H. Hibino

Symmetrization of diffraction peak profiles measured with a high-resolution synchrotron X-ray powder diffractometer

T. Ida* and H. Hibino

Ceramics Research Laboratory, Nagoya Institute of Technology, Asahigaoka, Tajimi, 507-0071, Japan. Correspondence e-mail: ida.takashi@nitech.ac.jp

The asymmetry of diffraction peak profiles observed with a high-resolution synchrotron powder X-ray diffractometer has been successfully removed by a double deconvolution method. In the first step, the asymmetry caused by the axial divergence aberration of the diffractometer is removed by a whole-pattern deconvolution method based on an *a priori* theoretical model for the aberration. In the second step, the residual asymmetry, the origin of which can be ascribed to the aberrations of the beamline optics, is also removed by a whole-pattern deconvolution method, based on an empirical model derived from the analysis of experimental diffraction peak profiles of a standard Si powder (NIST SRM640b). The beamline aberration has been modelled by the convolution of a pseudo-Voigt or Voigt function with an exponential distribution function. It has been found that the angular dependence of the asymmetry parameter in the exponential function is almost proportional to $\tan\theta$, which supports the idea that the residual asymmetry should be ascribed mainly to the intrinsic asymmetry in the spectroscopic distribution of the source X-ray supplied by the beamline optics of the synchrotron facility. Recently developed procedures of whole-pattern deconvolution have been improved to treat the singularity of the instrumental function in the measured angular range. Formulae for the whole-pattern deconvolution based on the Williamson–Hall-type dependence of the width parameter of the instrumental function have also been developed. The method was applied to the diffraction intensity data of a standard ZnO powder sample (NIST SRM674) measured with a high-resolution powder diffractometer on beamline BL4B$_2$ at the Photon Factory. The structure parameters of ZnO were refined from the integrated peak intensities, which were extracted by an individual profile fitting method applying symmetric profile models. The refined structure parameters coincide fairly well with those obtained from single-crystal data.

1. Introduction

Previously, we have reported the exact theoretical formulae of the axial-divergence aberration function for a high-resolution synchrotron X-ray powder diffractometer with a crystal analyser (Ida *et al.*, 2001), and also proposed an analytical method based on a Fourier analysis to remove the aberration from the observed data (Ida, Hibino & Toraya, 2003). The peak profiles obtained by the deconvolution of the axial-divergence aberration have shown residual asymmetry, which could be ascribed to the aberration of the monochromator and focusing optics on the beamline (beamline aberration). However, the origin of the residual asymmetry was not clear, except that the dependence of the residual asymmetry on the diffraction angles was found to be almost linear within a limited angular range of $10 \leq 2\Theta \leq 40°$.

The application of the deconvolution method was restricted to the low-angle data in our previous study, partly because the original formula of the whole-pattern deconvolution with abscissa-scale transformation (Ida, Hibino & Toraya, 2003) for the axial-divergence aberration with a crystal analyser with a Bragg angle of Θ_A has a singularity at the diffraction angle $2\Theta = 90° + \Theta_A$, which means that an infinitely large number of temporary data would be required near the singular point on the numerical process. Furthermore, interpretation of the data measured with a multiple-detector system (MDS) on beamline BL4B$_2$ at the Photon Factory was complicated because of the possible differences in the instrumental functions of different detectors.

Recently, we have developed an automatic method to adjust the variation of the instrumental functions of multiple detectors (Ida, 2005), which greatly simplifies the interpretation of the data measured with the MDS.

In this study, a modified formula for the whole-pattern deconvolution, which can be applied to remove the axial-divergence aberration from all the diffraction intensity data over the singular point, has been developed. Eleven diffraction peak profiles of a standard Si powder (NIST SRM674b) in the range $24.0 \leq 2\Theta \leq 148.4°$, measured at a wavelength of $\lambda = 1.306$ Å, are analysed in detail. The formula for removing the beamline aberration is modified according to the results of the detailed analysis of the diffraction peak profiles of the standard sample. The improved deconvolution methods to remove the axial-divergence and beamline aberrations are applied to the diffraction intensity data of a standard ZnO powder (NIST SRM674), measured in a multiple-detector mode, and the symmetric features of the experimental peak profiles are discussed.

2. Theory

2.1. Axial-divergence aberration function

The effect of axial divergence, limited by a set of Soller slits on the diffracted-beam side of the goniometer, is the only significant aberration arising from the optics of a high-resolution synchrotron X-ray powder diffractometer (Ida *et al.*, 2001). The instrumental function for the axial-divergence aberration is given by

$$\omega_A(\Delta 2\theta) = \begin{cases} |\beta_A|^{-1}[(-\Delta 2\theta/\beta_A)^{-1/2} - 1] \\ \qquad \text{for } -1 < \Delta 2\theta/\beta_A < 0, \\ 0 \qquad \text{elsewhere,} \end{cases} \tag{1}$$

with

$$\beta_A = (\Phi^2/2)(\cot 2\theta + \tan \Theta_A), \tag{2}$$

where Φ is the full width at half-maximum (FWHM) of the angular distribution of the axially divergent beam restricted by the Soller slits, and Θ_A is the Bragg angle at the crystal analyser (Ida *et al.*, 2001). Note that the instrumental function approaches the Dirac delta function at the singular point $2\Theta_s = \pi/2 + \Theta_A$, where the characteristic width β_A of the aberration function approaches zero. The above formulae are valid for both positive and negative value of β_A; that is, they cover all the possible diffraction angles, $0 < 2\theta < \pi$, including the range $\pi/2 + \Theta_A < 2\theta < \pi$, except the singular point at $2\Theta_s$.

Although the width of the instrumental function depends on the diffraction angle 2θ, abscissa-independent formulae of the instrumental function can be derived by applying the following function for the scale transformation about the abscissa from 2θ to χ (Ida & Toraya, 2002):

$$\chi = G_A(2\theta)$$
$$= (2\theta \sin \Theta_A - \cos \Theta_A \ln | \sin 2\theta \tan \Theta_A + \cos 2\theta|)$$
$$\times (2/\Phi^2) \cos \Theta_A, \tag{3}$$

for $0 < 2\theta < 2\Theta_s$, and

$$\chi = G_A(2\theta)$$
$$= - (2\theta \sin \Theta_A - \cos \Theta_A \ln | \sin 2\theta \tan \Theta_A + \cos 2\theta|)$$
$$\times (2/\Phi^2) \cos \Theta_A, \tag{4}$$

for $2\Theta_s < 2\theta < \pi$, both of which satisfy the following relation:

$$\Delta \chi/\Delta 2\theta = 1/|\beta_A|. \tag{5}$$

This means that the width and the shape of the aberration function become constant on the transformed scale χ on the abscissa.

The scale-transform function $G_A(2\theta)$ diverges to ∞ and $-\infty$ at the singular point $2\Theta_s$ for the ranges $2\theta < 2\Theta_s$ and $2\Theta_s < 2\theta$, respectively. The singularity or infinity can be avoided by separating the data into three parts in numerical calculations, namely the lower- and higher-angle regions, and the intermediate region around $2\theta \simeq 2\Theta_s$. The method to treat the intermediate region is discussed in the following section in detail.

The abscissa-independent formula of the instrumental function is then given by

$$w_A(\Delta \chi) = \begin{cases} (-\Delta \chi)^{-1/2} - 1 \\ \qquad \text{for } -1 < \Delta \chi < 0, \\ 0 \qquad \text{elsewhere,} \end{cases} \tag{6}$$

for $2\theta < 2\Theta_s$, and

$$w_A(\Delta \chi) = \begin{cases} (\Delta \chi)^{-1/2} - 1 \\ \qquad \text{for } 0 < \Delta \chi < 1, \\ 0 \qquad \text{elsewhere,} \end{cases} \tag{7}$$

for $2\theta > 2\Theta_s$.

The Fourier transform of the abscissa-independent instrumental function $w_A(\chi)$, defined by

$$W_A(\xi) = \int_{-\infty}^{\infty} w_A(\chi) \exp(2\pi i \xi \chi) d\chi,$$

for the range $2\theta < 2\Theta_s$ is given by

$$W_A(\xi) = \xi^{-1/2}[C(2\xi^{1/2}) - iS(2\xi^{1/2})]$$
$$- (2\pi i\xi)^{-1}[1 - \exp(-2\pi i\xi)], \tag{8}$$

for $\xi > 0$, and

$$W_A(\xi) = |\xi|^{-1/2}[C(2|\xi|^{1/2}) + iS(2|\xi|^{1/2})]$$
$$- (2\pi i\xi)^{-1}[1 - \exp(-2\pi i\xi)] \tag{9}$$

for $\xi < 0$, where $C(x)$ and $S(x)$ are the Fresnel functions defined by

$$C(x) \equiv \int_0^x \cos(\pi t^2/2) \, dt \tag{10}$$

and

$$S(x) \equiv \int_0^x \sin(\pi t^2/2) \, dt. \tag{11}$$

The Fourier formulae for $2\theta > 2\Theta_s$ are simply given by the Hermite conjugate of $W_A(\xi)$ for $2\theta < 2\Theta_s$.

research papers

2.2. Treatment of the singularity in the axial-divergence aberration function

The axial-divergence aberration function $\omega_A(\Delta 2\theta)$ has non-zero values only in the range $-|\beta_A| < \Delta 2\theta < 0$ for $2\theta < 2\Theta_s$, and $0 < \Delta 2\theta < |\beta_A|$ for $2\theta > 2\Theta_s$, as shown in equation (1). Then the maximum width of the function $\omega_A(\Delta 2\theta)$ immediately corresponds to the value

$$|\beta_A| = (\Phi^2/2)|\cot 2\theta + \tan \Theta_A|,$$

which can be approximated for a small deviation from $2\Theta_s$ as

$$|\beta_A| \simeq \Phi^2|2\theta - 2\Theta_s|/2\cos^2\Theta_A. \tag{12}$$

If the width of the instrumental function is much narrower than the interval of the measurement step, the convolution or deconvolution of the instrumental function will not affect the intensity profiles, practically. In the current method, the data in the range where the width of the instrumental function is narrower than 1/10 of the measurement step are left unchanged and simply combined with the deconvoluted data in the lower- and higher-angle ranges. Actually, the width of the axial-divergence instrumental function was narrower than $0.0005°$ in the range $98.4 < 2\theta < 104.6°$, for $\Phi = 1°$ and $\Theta_A = 11.535°$. The scheme for the segmentation, deconvolution and combination of data is illustrated in Fig. 1.

2.3. Asymmetry caused by the beamline aberration

The asymmetry caused by the beamline aberration is modelled by the convolution with an exponential distribution function with the following form (Ida, Hibino & Toraya, 2003):

$$\omega_E(\Delta 2\theta) = \begin{cases} |\alpha|^{-1}\exp(-\Delta 2\theta/\alpha) \\ \qquad \text{for } \Delta 2\theta/\alpha > 0, \\ 0 \qquad \text{elsewhere.} \end{cases} \tag{13}$$

The parameter α can be treated as the measure of asymmetry. The longer tail on the lower- or higher-angle side of a peak corresponds to the negative or positive sign of α, respectively.
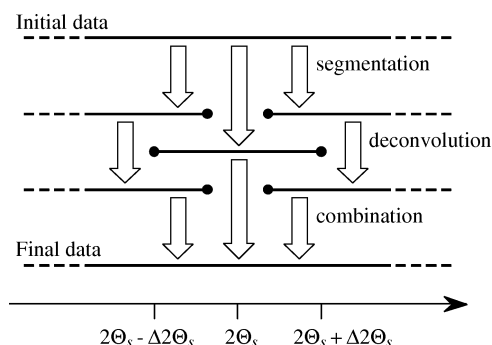

Figure 1
Scheme for treating data near the singular point $2\Theta_s$ of instrumental functions in the whole-pattern deconvolution method. Three sets of partly overlapping segmented data are created from the initial data. The lower- and higher-range data are treated by deconvolution and combined with the middle-range data, $2\Theta_s - \Delta 2\Theta_s \leq 2\theta \leq 2\Theta_s + \Delta 2\Theta_s$, where the width of the instrumental function is narrower than 1/10 of the measurement step interval. The data are combined again by calculating weighted averages of data in the overlapped regions.

When the angular dependence of α is assumed to be given by

$$\alpha = \gamma_E(2\theta) = \alpha_X \sec\theta + \alpha_Y \tan\theta, \tag{14}$$

which is identical to the Williamson–Hall-type dependence on the diffraction angle (Williamson & Hall, 1953), singularity may appear at $\sin\theta = -\alpha_X/\alpha_Y$ for the case $\alpha_Y/\alpha_X < -1$. Formally, the singular point $2\Theta_s$ is calculated by

$$2\Theta_s = -2\arcsin(\alpha_X/\alpha_Y) \tag{15}$$

for $\alpha_Y/\alpha_X < -1$. The formulae for the scale transform, the abscissa-independent instrumental functions and the Fourier transform are given by

$$G_E(2\theta) = (2/\alpha_Y)\ln|\alpha_X/\alpha_Y + \sin\theta|, \tag{16}$$

$$w_E(\chi) = \begin{cases} \exp(-x) & \text{for } x > 0, \\ 0 & \text{elsewhere,} \end{cases} \tag{17}$$

$$W_E(\xi) = 1/(1 - 2\pi i\xi) \tag{18}$$

for the case $\alpha > 0$, and

$$G_E(2\theta) = -(2/\alpha_Y)\ln|\alpha_X/\alpha_Y + \sin\theta|, \tag{19}$$

$$w_E(\chi) = \begin{cases} \exp(x) & \text{for } x < 0, \\ 0 & \text{elsewhere,} \end{cases} \tag{20}$$

$$W_E(\xi) = 1/(1 + 2\pi i\xi) \tag{21}$$

for the case $\alpha < 0$.

If necessary, the possible singularity would be treated by the segmentation–deconvolution–combination scheme described in the preceding section.

2.4. Removal of asymmetry

Assuming the Williamson–Hall-type dependence, the asymmetry caused by the beamline aberration would be removed by deconvolution with an appropriate scale transformation as shown in §2.3. However, the deconvolution generally causes an increase of noise to compensate for the sharpened peak profiles in the deconvoluted data. Furthermore, there is no theoretical basis for the assumption that the exponential formula should be used as the model for the asymmetry caused by the beamline optics, while the formula for the axial-divergence aberration has unambiguously been derived from the geometry of the optics and the theory of diffraction.

In order to suppress the increase of noise, and also to reduce changes in the characteristics of the peak profiles, except the asymmetry, convolution with a symmetric function $w_S(\chi)$ with the Fourier form

$$W_S(\xi) = |W_E(\xi)|$$
$$= (1 + 4\pi^2\xi^2)^{-1/2} \tag{22}$$

is simultaneously applied with the deconvolution of $w_E(\chi)$. The symmetric function $w_S(\chi)$, defined as the inverse Fourier transform of $W_S(\chi)$, is simply given by

$$w_S(\chi) = \pi^{-1} K_0(\chi), \qquad (23)$$

where $K_0(x)$ is the modified Bessel function of the second kind.

3. Experimental

The powder diffraction data were collected with the multiple-detector system on beamline $BL4B_2$ at the Photon Factory in Tsukuba (Toraya *et al.*, 1996). The axial divergence of the diffracted beam was limited within $\Phi = 1°$ FWHM with a set of Soller slits.

The Bragg angle of the Ge(111) crystal analyser for the calibrated source X-ray wavelength of $\lambda = 1.306$ Å was estimated at $\Theta_A = 11.535°$.

Standard Si powder (NIST SRM640b), filled into the hollow of the flat-plate specimen holder of diameter 30 mm, was used to evaluate the instrumental functions of the measurement system, which may be affected by the spectroscopic intensity distribution of the source X-ray. The specimen was rotated about its surface normal at one revolution s^{-1} during the measurement.

The diffraction intensity data of 11 reflection peaks from the standard Si specimen were collected with a single-detector 2Θ scan mode, using one of the multiple detectors. The step interval of the 2Θ scan was $0.005°$. The measurement time at each step was 1 s for the 111, 220, 311, 400 and 422 reflections, and 8 s for the 711/551, 642, 731/553 and 800 reflections.
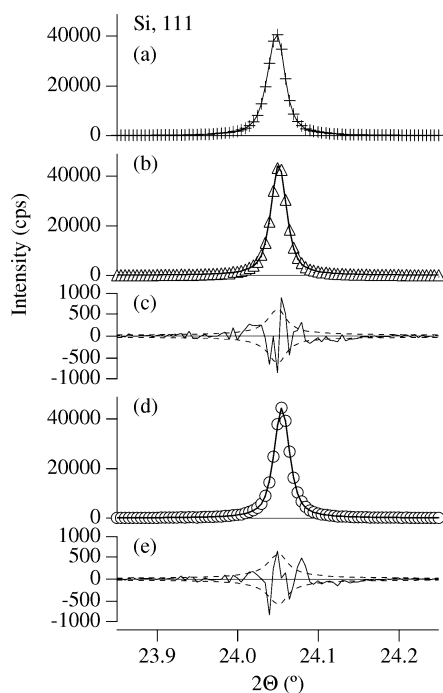
The counting losses caused by the finite response time of the detector system were corrected by an intermediately extended dead-time model (Ida & Iwata, 2005).

A flat-plate specimen of standard ZnO powder (NIST SRM674) was used as a test sample for the current method to symmetrize the experimental diffraction peak profiles. The diffraction data, ranging from -1.43 to $154.98°$ in 2Θ, were collected by a MDS measurement method. The measurement time at each step was 4 s. Further details of the apparatus, the measurement conditions for the ZnO specimen and the method to connect the segmented intensity data from the multiple detectors, have been described elsewhere (Ida, 2005).

4. Analysis

4.1. Calibration of instrumental characteristics

4.1.1. Evaluation of asymmetry. In a first step, the aberrations caused by the divergence of the diffracted beam along the axial direction were removed from the Si diffraction intensity data by a deconvolution method recently developed by the authors (Ida, Hibino & Toraya, 2003) but with application of the modification described here in §2.2. The results of the deconvolution of axial divergence applied to the 111 and 711/551 reflection data are shown as triangles in Figs. 2(b) and 3(b).

After the removal of the axial-divergence aberrations, slight asymmetry of the diffraction peak profiles still remained, similarly to our previous results (Ida, Hibino & Toraya, 2003). The asymmetric deconvoluted profiles were fitted with an asymmetric function defined by the convolution of a pseudo-

Figure 2
The 111 peak profiles of standard Si (NIST SRM640b) powder. (*a*) Raw intensity profile; (*b*) deconvoluted profile (triangles) and the fitted asymmetrized pseudo-Voigt function; (*c*) difference plot of the fitting shown in (*b*); (*d*) symmetrized profile (circles) and the fitted pseudo-Voigt function; (*e*) difference plot of the fitting shown in (*d*). In the difference plots, statistical uncertainties calculated based on counting statistics are shown as broken lines.
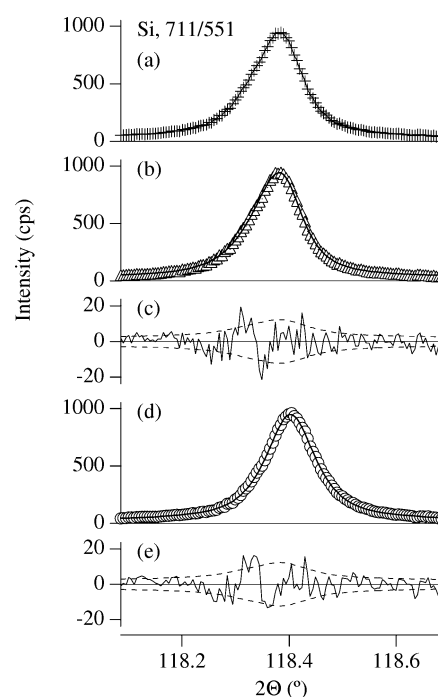

Figure 3
The 711/551 peak profiles of standard Si (NIST SRM640b) powder. See the caption of Fig. 2 for definitions.

T. Ida and H. Hibino · Symmetrization of diffraction peak profiles **93**

Table 1
Profile parameters of the deconvoluted Si standard diffraction peaks fitted with asymmetrized pseudo-Voigt function.

hkl	b	S	$2\theta_0$ (°)	Γ_S (°)	η	α (°)	R_p (%)	R_{wp} (%)
111	21 (7)	1459 (9)	24.0546 (3)	0.0208 (5)	0.829 (17)	−0.0038 (4)	2.12	4.26
220	47 (4)	1080 (4)	39.7856 (2)	0.0266 (4)	0.876 (14)	−0.0067 (3)	1.74	3.26
311	49 (5)	654 (4)	47.0296 (5)	0.0307 (9)	0.882 (3)	−0.0081 (5)	2.90	4.37
400	26 (3)	186 (2)	57.5243 (10)	0.0395 (17)	0.888 (4)	−0.0091 (11)	3.95	6.13
422	55 (4)	451 (2)	72.2169 (4)	0.0429 (7)	0.813 (19)	−0.0143 (4)	2.26	3.79
440	32.7 (9)	142.9 (6)	85.7589 (3)	0.0518 (6)	0.812 (14)	−0.0171 (3)	1.54	2.62
533	27.3 (11)	84.5 (7)	104.1382 (5)	0.0701 (10)	0.77 (2)	−0.0226 (6)	1.85	2.43
711/551	29.5 (8)	144.8 (7)	118.4025 (5)	0.0877 (11)	0.873 (16)	−0.0307 (6)	1.76	2.55
642	38.5 (17)	254.4 (16)	128.3363 (6)	0.1044 (13)	0.826 (19)	−0.0382 (7)	1.84	2.57
731/553	33.3 (8)	191.9 (10)	134.9948 (6)	0.1215 (15)	0.844 (17)	−0.0450 (8)	1.94	2.72
800	21.1 (10)	35.2 (13)	148.388 (3)	0.189 (7)	0.88 (8)	−0.060 (4)	4.89	6.01

Table 2
Profile parameters of the deconvoluted Si standard diffraction peaks fitted with the asymmetrized extended pseudo-Voigt function.

hkl	b	S	$2\theta_0$ (°)	Γ_L (°)	Γ_G	α (°)	R_p (%)	R_{wp} (%)
111	32 (7)	1453 (9)	24.0542 (4)	0.01633 (17)	0.0099 (6)	−0.0034 (4)	1.95	4.00
220	54 (4)	1075 (4)	39.7855 (3)	0.0225 (3)	0.0101 (9)	−0.0066 (3)	1.84	3.40
311	53 (6)	651 (5)	47.0296 (5)	0.0261 (9)	0.0114 (17)	−0.0081 (6)	2.94	4.48
400	28 (3)	185 (2)	57.5242 (10)	0.0336 (13)	0.15 (3)	−0.0089 (11)	3.90	6.13
422	62 (4)	446 (3)	72.2169 (4)	0.0323 (8)	0.0207 (14)	−0.0143 (5)	2.31	3.86
440	35.2 (11)	141.0 (7)	85.7590 (3)	0.0385 (7)	0.0257 (12)	−0.0172 (4)	1.58	2.70
533	29.5 (12)	82.7 (7)	104.1382 (5)	0.0475 (17)	0.040 (2)	−0.0226 (6)	1.84	2.45
711/551	30.8 (9)	143.3 (9)	118.4026 (5)	0.0720 (15)	0.036 (3)	−0.0308 (6)	1.82	2.60
642	41.9 (19)	250.0 (19)	128.3365 (6)	0.078 (2)	0.052 (3)	−0.0384 (7)	1.89	2.60
731/553	34.9 (9)	189.3 (12)	134.9949 (6)	0.095 (2)	0.056 (3)	−0.0451 (8)	1.94	2.76
800	21.3 (11)	34.8 (15)	148.388 (3)	0.156 (18)	0.08 (2)	−0.060 (4)	4.59	6.00

Voigt function with an asymmetric exponential function $\omega_E(\Delta 2\theta)$ given in §2.3. The pseudo-Voigt function is defined by

$$f_{pV}(x;\ \Gamma_S, \eta) = (1 - \eta)f_G[x;\ \Gamma_S/2(\ln 2)^{1/2}] + \eta f_L(x;\ \Gamma_S/2),$$
(24)

where $f_G(x;\ \gamma_G)$ is the Gaussian function given by

$$f_G(x;\ \gamma_G) = \pi^{-1/2}\gamma_G^{-1}\exp(-x^2/\gamma_G^2),$$
(25)

and $f_L(x;\ \gamma_L)$ is the Lorentzian function given by

$$f_L(x;\ \gamma_L) = \pi^{-1}\gamma_L/(\gamma_L^2 + x^2).$$
(26)

The constant background b, integrated intensity S, peak position $2\theta_0$, FWHM of the symmetric component Γ_S, shape parameter for the pseudo-Voigt function η, and the asymmetry parameter α in the asymmetric component function, are treated as adjustable profile parameters to be optimized.

Figs. 2(b), 2(c), 3(b) and 3(c) show the results of fitting and difference plots. The optimized profile parameters for the 11 reflection of Si are listed in Table 1. The R factors defined by

$$R_p = \sum_i |y_i(\text{obs.}) - y_i(\text{calc.})|/\sum_i |y_i(\text{obs.})|$$
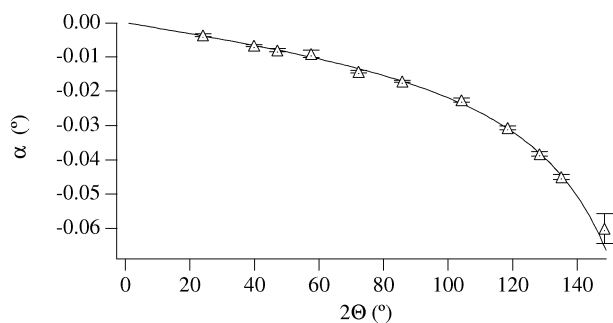(27)

and

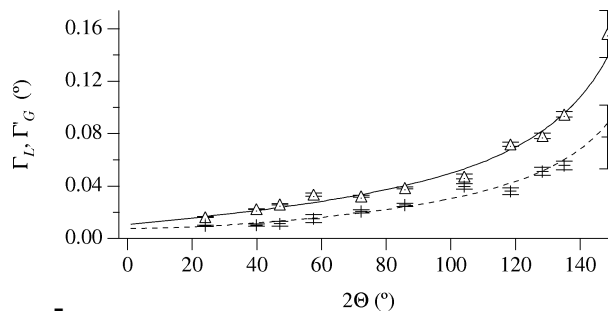**Figure 4**
The angular dependence of the asymmetry parameter α for the measurement of Si powder (triangles). The optimized Williamson–Hall-type dependence is shown as a solid curve.

Figure 5
The angular dependence of the Lorentzian width Γ_L (triangles) and the Gaussian width Γ_G (crosses) of the Voigtian profile assigned to the symmetric part of the deconvoluted diffraction peak profile of Si powder, evaluated by profile fitting with asymmetrized Voigt profiles to the data after deconvolution of axial divergence aberration. The optimized dependences obtained by a non-linear fitting procedure are shown as solid and broken curves, respectively.

Table 3
Profile parameters for the symmetrized Si diffraction peaks individually fitted with a pseudo-Voigt function.

hkl	b	S	$2\theta_0$ (°)	Γ_S (°)	η	R_p (%)	R_{wp} (%)
111	15 (6)	1463 (8)	24.05478 (7)	0.0232 (2)	0.770 (13)	2.18	3.86
220	31 (4)	1089 (4)	39.78555 (6)	0.0317 (2)	0.80 (9)	1.60	2.96
311	37 (5)	662 (4)	47.02953 (13)	0.0369 (5)	0.805 (17)	2.72	3.84
400	24 (4)	188 (2)	57.5252 (2)	0.0460 (8)	0.83 (3)	3.52	4.78
422	40 (3)	462 (2)	72.21623 (12)	0.0537 (4)	0.763 (13)	2.32	3.46
440	26.8 (9)	147.5 (6)	85.75891 (9)	0.0646 (3)	0.781 (9)	1.52	2.42
533	22.7 (10)	88.4 (7)	104.13891 (15)	0.0861 (5)	0.780 (15)	1.76	2.45
711/551	23.4 (8)	151.8 (8)	118.40265 (16)	0.1118 (6)	0.850 (10)	1.67	2.34
642	23 (2)	272.1 (19)	128.3361 (2)	0.1337 (8)	0.846 (13)	1.97	3.21
731/553	26.1 (8)	202.8 (10)	134.9944 (2)	0.1564 (8)	0.842 (10)	1.78	2.47
800	18.4 (11)	39.5 (15)	148.3912 (9)	0.239 (4)	0.94 (5)	3.84	4.94

Table 4
Profile parameters for the symmetrized Si diffraction peaks individually fitted with the Voigt function.

hkl	b	S	$2\theta_0$ (°)	Γ_L (°)	Γ_G (°)	R_p (%)	R_{wp} (%)
111	31 (5)	1454 (7)	24.05477 (6)	0.0165 (2)	0.0122 (4)	1.93	3.37
220	45 (4)	1080 (4)	39.78555 (7)	0.0234 (3)	0.0159 (5)	1.79	3.00
311	47 (6)	655 (5)	47.02951 (14)	0.0274 (6)	0.0184 (10)	2.87	3.91
400	27 (3)	186 (2)	57.5252 (2)	0.0350 (8)	0.0221 (17)	3.43	4.66
422	50 (4)	454 (3)	72.21622 (14)	0.0365 (8)	0.0302 (11)	2.40	3.48
440	30.0 (13)	144.8 (8)	85.75891 (12)	0.0451 (8)	0.0351 (11)	1.78	2.57
533	24.2 (12)	86.8 (8)	104.13889 (16)	0.0599 (15)	0.0471 (17)	1.86	2.55
711/551	24.8 (10)	150.0 (10)	118.40266 (19)	0.0881 (15)	0.051 (2)	1.95	2.51
642	25 (2)	269 (2)	128.3361 (3)	0.105 (2)	0.061 (3)	2.23	3.35
731/553	27.4 (10)	200.1 (13)	134.9944 (3)	0.122 (2)	0.073 (3)	1.95	2.62
800	18.1 (10)	39.7 (14)	148.3912 (9)	0.221 (14)	0.06 (2)	3.83	4.95

$$R_{wp} = \left[\sum_i w_i |y_i(\text{obs.}) - y_i(\text{calc.})|^2 \right]^{1/2} \times \left[\sum_i w_i y_i^2(\text{obs.}) \right]^{-1/2}, \quad (28)$$

where w_i is the weight for the least-squares fitting, are also listed in the table.

The optimized value of asymmetry parameter α for each reflection is plotted *versus* the diffraction angle in Fig. 4. The dependence of the asymmetry parameter α is fitted by the Williamson–Hall-type dependence given by equation (14). The optimized coefficients of the secant and tangent terms, α_X and α_Y, are

$$\alpha_X = 0.0000 \ (3)°,$$
$$\alpha_Y = -0.0184 \ (5)°.$$

The apparent asymmetry has almost a purely tangential dependence on 2θ, which supports the idea that it is caused by the spectroscopic distribution of the source X-ray supplied by the beamline optics.

The deconvoluted profiles were also analysed by fitting with a function calculated as the convolution of the extended-pseudo-Voigt function (Ida *et al.*, 2000), which is practically equivalent to the exact Voigt profile, with the asymmetric component function $\omega_E(\Delta 2\theta)$ as the profile model. The optimized profile parameters are listed in Table 2. The values of the asymmetry parameter α coincide reasonably with those

obtained from the profile fitting using the pseudo-Voigt function.

Fig. 5 shows the angular dependence of the Lorentzian and Gaussian FWHM values of the extended-pseudo-Voigt approximation to the Voigt profile assigned to the symmetric part of the deconvoluted profile. The angular dependences of the Lorentzian and Gaussian widths are assumed to be expressed by the following equations:

$$\Gamma_L = \Gamma_{LX} \sec\theta + \Gamma_{LY} \tan\theta, \quad (29)$$

and

$$\Gamma_G^2 = \Gamma_{GX}^2 \sec^2\theta + \Gamma_{GY}^2 \tan^2\theta. \quad (30)$$

The optimized values of the coefficients, Γ_{LX}, Γ_{LY}, Γ_{GX} and Γ_{GY} are

$$\Gamma_{LX} = 0.0105 \ (3)°,$$
$$\Gamma_{LY} = 0.0281 \ (7)°,$$
$$\Gamma_{GX} = 0.0077 \ (4)°,$$
$$\Gamma_{GY} = 0.0235 \ (5)°.$$

The coefficients of the secant terms, Γ_{LX} and Γ_{GX}, should be unaffected during the removal of the asymmetric component, because the asymmetry has purely tangential dependence. If the secant terms of the Lorentzian and Gaussian components are assigned to isotropic size broadening of spherical crystallites, the area- and volume-weighted average diameters are formally estimated at

Table 5
Profile parameters for the symmetrized Si diffraction peaks fitted with the Voigt function with $\Gamma_{LX} = 0.0082°$, $\Gamma_{LY} = 0.0398°$, $\Gamma_{GX} = 0.0105°$ and $\Gamma_{GY} = 0.0311°$.

hkl	b	S	$2\theta_0$ (°)	Γ_L (°)	Γ_G (°)	R_p (%)	R_{wp} (%)
111	25 (7)	1457 (11)	24.05473 (11)	0.01685	0.01260	2.75	3.77
220	49 (4)	1078 (4)	39.78556 (7)	0.02310	0.01583	1.90	3.07
311	57 (6)	648 (6)	47.02963 (18)	0.02624	0.01771	3.63	4.73
400	37 (3)	179 (3)	57.5255 (4)	0.03117	0.02083	5.90	7.51
422	40 (3)	461 (2)	72.21628 (13)	0.03914	0.02612	2.57	3.75
440	25.7 (7)	147.5 (5)	85.75888 (12)	0.04810	0.03221	1.82	2.78
533	20.8 (5)	89.0 (3)	104.13884 (16)	0.06434	0.04337	1.95	2.70
711/551	28.2 (5)	146.6 (5)	118.4027 (2)	0.08269	0.05601	2.09	2.67
642	27.2 (11)	266.0 (11)	128.3359 (3)	0.10091	0.06855	2.47	3.44
731/553	28.9 (5)	198.1 (6)	134.9943 (3)	0.11735	0.07984	2.10	2.68
800	21.6 (3)	34.8 (3)	148.3913 (9)	0.17046	0.11629	3.96	5.18

$$\langle D \rangle_A = 340\ (9)\ \text{nm},$$
$$\langle D \rangle_V = 479\ (17)\ \text{nm}.$$

(see Appendix A).

4.1.2. Validation of the evaluated asymmetry. The Si diffraction peak profiles obtained by the deconvolution of the axial-divergence aberration from the observed profiles are symmetrized by the deconvolution of the exponential asymmetry followed by the convolution of the corresponding Bessel function, as described in §2.4. It should be noted that this process might not be necessary for analysis of the standard data for characterization of the instrument, but is useful for testing the validity of the analytical method. The angular dependence given by equation (14), and the values $\alpha_X = 0.0000°$ and $\alpha_Y = -0.0184°$ are applied.

The symmetrized diffraction peak profiles of Si 111 and 711/551 reflections are shown as circles in Figs. 2(d) and 3(d). The symmetrized profiles were fitted with the Voigt function, applying the numerical method proposed by Poppe & Wijers (1990), which is more accurate but takes more computation time than the extended-pseudo-Voigt approximation. The application of the more accurate formula is possible because there is no need for the calculation of the convolution with an asymmetric function for the analysis of the symmetrized profiles.
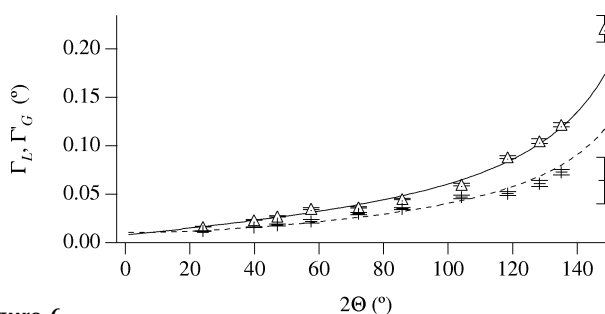
The profile parameters optimized by the individual Voigtian profile fittings are listed in Table 4.

Even though the uncertainties of the FWHM values of the Lorentzian and Gaussian components, Γ_L and Γ_G, optimized for the symmetrized profiles, are not significantly different from those obtained in §4.1.1, the effect of mutual correlation between Γ_L and Γ_G appears more pronounced here, as can be seen in Table 4 and the plot in Fig. 5. It suggests the degradation of the deconvoluted data, which may be caused by the neglect of the off-diagonal elements of the error matrix (Ida & Toraya, 2002).

Therefore, an iterative profile fitting procedure was performed, applying the constraints given by equations (29) and (30). The optimized values of the coefficients, Γ_{LX}, Γ_{LY}, Γ_{GX} and Γ_{GY} are

$$\Gamma_{LX} = 0.0082\ (4)°,$$
$$\Gamma_{LY} = 0.0398\ (8)°,$$
$$\Gamma_{GX} = 0.0105\ (6)°,$$
$$\Gamma_{GY} = 0.0311\ (7)°.$$

Figure 6
The angular dependence of the Lorentzian width Γ_L (triangles) and the Gaussian width Γ_G (crosses) of the Voigtian profile fitted to the symmetrized peak profile of Si powder, evaluated by profile fitting with the Voigt profile to the symmetrized data. The optimized dependences evaluated by a constrained profile fitting procedure are shown as solid and broken curves, respectively.
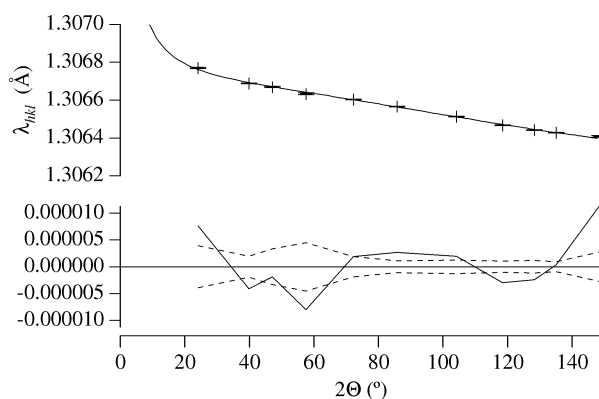

Figure 7
Validation of the calibrated wavelength and systematic errors. The nominal wavelength λ_{hkl} (crosses) and the values calculated by the optimized model for systematic errors (solid line) are shown in the upper part. The lower part shows the difference plot (solid line) with the errors (broken lines) evaluated from the results of the profile fitting.
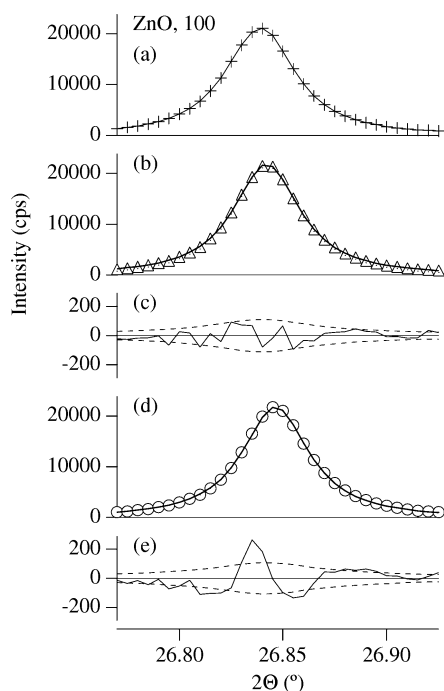
electronic reprint

Figure 8
The 100 peak profiles of ZnO (NIST SRM674) powder. See the caption of Fig. 2 for definitions.
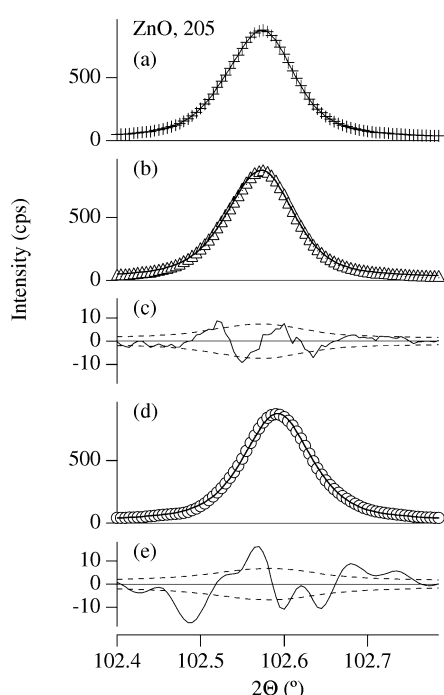

Figure 9
The 205 peak profiles of ZnO powder. See the caption of Fig. 2 for definitions.
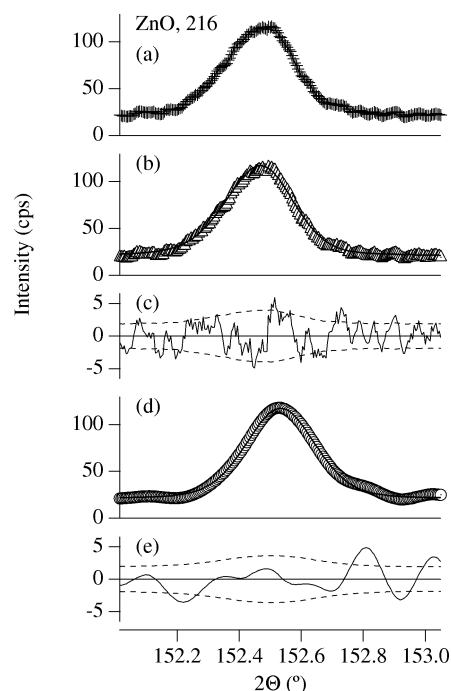
Figure 10
The 216 peak profiles of ZnO powder. See the caption of Fig. 2 for definitions.

The above values of the coefficients for the tangent terms, Γ_{LY} and Γ_{GY}, should be affected by the convolution with the Bessel function for smoothing, and be reasonably larger than the values estimated in the preceding section. The values of the secant-term coefficients, Γ_{LX} and Γ_{LY}, are again attributed to

the size broadening of spherical crystallites, and the area- and volume-weighted averages are estimated at

$$\langle D \rangle_A = 440\ (20)\ \text{nm},$$
$$\langle D \rangle_V = 490\ (20)\ \text{nm}.$$

The dependences calculated by the above parameters are drawn as lines in Fig. 6. The profile parameters optimized with the constraints are listed in Table 5. The changes in the optimized profile parameters or R values on application of the constraints are not significant, except the increase in the R values of the 400 reflection of Si, which can be caused by the intrinsically broader line width of the 400 reflection compared with the value calculated on the assumption of isotropic broadening.

4.1.3. Calibration of wavelength and systematic errors of the goniometer. Assuming the certified lattice constant of the standard Si powder (NIST SRM640b), $a = 5.430940\ (34)$ Å, the peak wavelengths for the symmetrized peak profiles are evaluated by a least-squares method. The optimized peak positions obtained by the fitting with the pseudo-Voigt function to the symmetrized profiles, listed in Table 3, are used to evaluate the wavelength.

The following model for systematic errors is assumed:

$$2\theta_{hkl} = 2\Theta_{hkl} - \Delta 2\Theta_0 - \Delta 2\Theta_1 \cos(2\Theta_{hkl} - 2\Theta_2), \quad (31)$$

where $2\theta_{hkl}$ is the true diffraction angle related to the wavelength λ by the Bragg equation,

$$\lambda = 2a(h^2 + k^2 + l^2)^{-1/2} \sin\theta_{hkl}, \quad (32)$$

Table 6
Structure parameters of ZnO.

	This work	Abrahams & Bernstein (1969)	Albertsson & Abrahams (1989)
Specimen	Powder	Single crystal	Single crystal
Source	Synchrotron X-ray	Laboratory X-ray	Neutron
No. of reflections	42	141	394
$z(O)$	0.3827 (8)	0.3825 (14)	0.3819 (1)
$U(Zn)$ (Å^2)		0.0080 (3)	
$U(O)$ (Å^2)		0.0086 (9)	
$U_{11}(Zn)$ (Å^2)	0.0079 (2)		0.0073 (4)
$U_{33}(Zn)$ (Å^2)	0.0080 (4)		0.0094 (4)
$U_{11}(O)$ (Å^2)	0.0065 (11)		0.0056 (4)
$U_{33}(O)$ (Å^2)	0.0095 (21)		0.0064 (4)
R (%)	0.85	3.78	2.31
R_w (%)	1.57	5.12	3.67

$2\Theta_{hkl}$ is the observed peak position, and $\Delta2\Theta_0$, $\Delta2\Theta_1$, $2\Theta_2$ are parameters for modelling mechanical systematic errors of the goniometer. The second term in equation (31) models a constant offset error, and the third term models a deviation with the periodicity of 360°, which may be assigned to a gear eccentricity error (Toraya *et al.*, 1993; Hart *et al.*, 1990).

The optimized peak wavelength, offset and eccentricity errors are estimated at

$$\lambda = 1.306348\ (12)\ \text{Å},$$
$$\Delta2\Theta_0 = 0.006\ (2)^\circ,$$
$$\Delta2\Theta_1 = 0.0122\ (6)^\circ,$$
$$2\Theta_2 = 107\ (8)^\circ.$$

In order to examine the appropriateness of the assumed systematic errors, the nominal wavelength λ_{hkl} calculated from each peak position $2\Theta_{hkl}$ by

$$\lambda_{hkl} = 2d_{hkl}\sin\Theta_{hkl}, \qquad (33)$$

and the curve calculated by

$$\lambda'(2\Theta) = (\lambda/\sin\Theta)\sin[\Theta + \Delta2\Theta_0/2$$
$$+ (\Delta2\Theta_1/2)\cos(2\Theta - 2\Theta_2)], \qquad (34)$$

are compared in Fig. 7. It has been confirmed that good coincidence is achieved by the above model for mechanical systematic errors.

When the strain broadening is assumed to be negligible in the standard Si powder, the tangent terms in equation (14) are assigned to the spectroscopic distribution of the source X-ray, while the secant terms in equations (29) and (30) are connected with the size broadening of the Si crystallites.

4.2. Analysis of ZnO powder diffraction data

4.2.1. Deconvolution of axial-divergence aberration. The effect of the axial-divergence aberration has been removed from the powder diffraction intensity data of ZnO by a modified algorithm for the whole-pattern deconvolution method, as described in §2.2.

The singular point of the aberration function is located at $2\Theta_s = 90° + \Theta_A = 101.54°$. By applying equation (12) for the tolerable width of the aberration function, 0.0005°, which is 1/
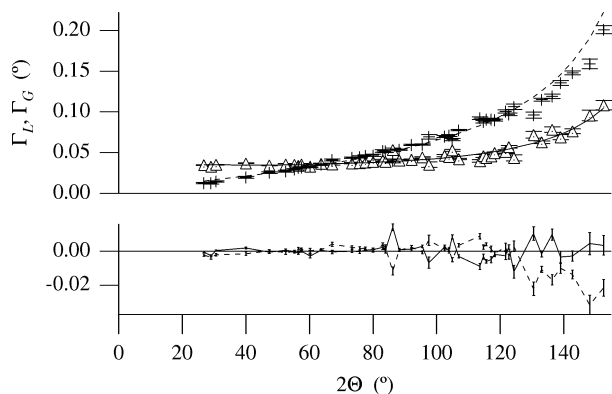

Figure 11
The Lorentzian (triangles) and Gaussian (crosses) FWHM values of the ZnO diffraction peaks. The optimized and difference curves are shown in the upper and lower panels, respectively.
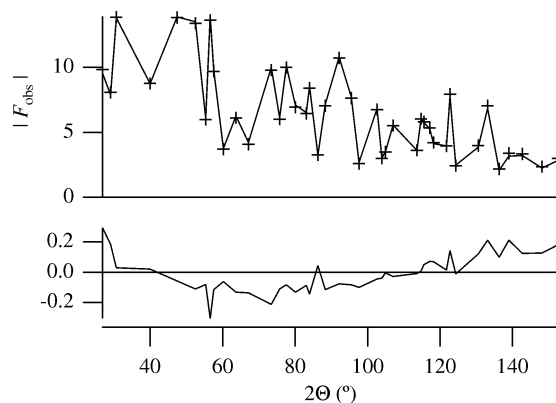

Figure 12
The structure factor $|F|$ of ZnO powder. The experimental values are shown as crosses and the calculated values are drawn as a line in the upper part. The lower part shows the difference.

10 of the measurement step, the data ranging from 98.39° to 104.69° in 2Θ are assumed to be unaffected by the axial-divergence aberration. The lower-angle data below 100.49° and the higher-angle data above 102.59° were separately treated by the original whole-pattern deconvolution method (Ida, Hibino & Toraya, 2003), and combined again with the original data in the range 98.39–104.69°.

Figs. 8–10 show the change in the peak profiles of the 100, 205 and 216 reflections of ZnO, through the deconvolution and symmetrization processes.

The effects of the deconvolution of the axial-divergence aberration are only significant in the low-angle range, as can be seen for the 100 reflection in Fig. 8. The asymmetry of the initial data is reduced and the peak position is shifted to the higher-angle side after the deconvolution of the axial-divergence effect.

The peak profile of the 205 reflection of ZnO located near the singular point $2\Theta_s$ is not changed in the deconvolution process. The higher-angle tail of the 216 reflection, located above $2\Theta_s$, is slightly reduced and the peak is shifted to the lower-angle side after the deconvolution of the axial-divergence aberration.

4.2.2. Symmetrization of the peak profiles. The asymmetry modelled by the convolution with an exponential distribution function was also removed by the whole-pattern deconvolution method.

As can be seen in Figs. 8–10, the asymmetry of the diffraction peak profiles of the ZnO powder has certainly been removed by the symmetrization process. Shifts of the apparent peak positions through the symmetrization process are also observed. The peak positions of the symmetrized peak profiles naturally correspond to the hypothetical symmetric spectral distribution of the source X-ray, the peak position of which is located at $\lambda = 1.306348\ (12)$ Å. Note that the value of the peak wavelength was determined from the symmetrized peak profiles of the standard Si powder obtained by the same method.

The isotropic broadening model given by equations (29) and (30) is applied to fit the line-width parameters Γ_L and Γ_G evaluated by the individual peak profile fittings with the Voigt function to the symmetrized ZnO peak profiles. The results of the least-squares fitting are shown in Fig. 11. The optimized parameters are

$$\Gamma_{LX} = 0.0372\ (6),$$
$$\Gamma_{LY} = -0.0127\ (10),$$
$$\Gamma_{GX} = 0.0076\ (18),$$
$$\Gamma_{GY} = 0.054\ (2).$$

Even though the main features of the observed dependence are apparently reproduced by the above parameters, the negative sign of Γ_{LY} indicates that the isotropic broadening modelled by the combination of secant and tangent dependences is not reasonable for the angular dependence of the observed profiles.

4.2.3. Evaluation of lattice constants. The lattice constants of the ZnO sample are evaluated from the positions of the symmetrized diffraction peaks. The formula for the systematic errors given by equation (31) is again assumed, fixing the wavelength at $\lambda = 1.306348$ Å. The lattice parameters a and c, the constant shift $\Delta 2\Theta_0$, and parameters for the eccentricity errors $\Delta 2\Theta_1$ and $2\Theta_2$, are treated as variable parameters to fit the observed peak positions. The optimized values of the parameters are

$$a = 3.249847\ (18)\ \text{Å},$$
$$c = 5.20650\ (3)\ \text{Å},$$
$$\Delta 2\Theta_0 = 0.0036\ (9)^{\circ},$$
$$\Delta 2\Theta_1 = 0.0077\ (3)^{\circ},$$
$$2\Theta_2 = 88\ (5)^{\circ}.$$

The evaluated lattice constants coincide well with the literature values, $a = 3.24990\ (4)$ Å and $c = 5.20660\ (6)$ Å at 300 K, estimated by the Bond method (Albertsson & Abrahams, 1989).

4.2.4. Structure refinement. The structure parameters of ZnO are refined to fit the integrated peak intensities evaluated by application of the individual profile fitting method applying the Voigt function as the symmetric profile model. The enhancement factor for asymmetric reflection measurement (Toraya *et al.*, 1993), and a modified formula for March–Dollase preferred-orientation correction for asymmetric reflection (see Appendix B) have been applied. The linear absorption coefficients were calculated by using *X0h*, developed by Stepanov (2005).

The optimized structure parameters are listed in Table 6. All the parameters coincide well with the results obtained by single-crystal methods. The March–Dollase preferred-orientation parameter has been estimated at $r = 1.055\ (4)$, which means that the c axis of the crystallites has a slight tendency to orient parallel to the specimen face, which is reasonable because it is known that crystallites of ZnO are usually elongated along the c axis.

The observed and calculated values of the structure factors are shown in Fig. 12. The slight systematic deviation may be attributed to the change in electron charge density from the neutral atoms assumed for the applied atomic scattering factors.

5. Conclusion

A convenient method to symmetrize the diffraction peak profiles measured with a high-resolution powder diffractometer has been developed. Application of the symmetrization procedure has following advantages. (i) The integrated intensities of the peaks can be extracted by a simple curve fitting method with a symmetric profile function if the intrinsic diffraction peak profiles of the sample are symmetric. (ii) The observed peak position unambiguously corresponds to the calibrated peak wavelength, while it can be affected by broadening effects in the asymmetric case. (iii) Intrinsic asymmetry in diffraction peak profiles, which may be caused

research papers

by stacking faults for example, can properly be extracted from the experimental data.

APPENDIX A
Evaluation of average crystallite size from Voigtian profile parameters

The normalized Lorentzian and Gaussian functions are given by

$$f_L(x; \gamma_L) = (1/\pi\gamma_L)[1 + (x/\gamma_L)^2]^{-1} \qquad (35)$$

and

$$f_G(x; \gamma_G) = (1/\pi^{1/2}\gamma_G)\exp[-x^2/\gamma_G^2], \qquad (36)$$

the Fourier transforms of which are respectively given by

$$F_L(\xi; \gamma_L) = \exp(-2\pi|\xi|\gamma_L) \qquad (37)$$

and

$$F_G(\xi; \gamma_G) = \exp(-\pi^2\xi^2\gamma_G^2). \qquad (38)$$

The Fourier initial slope of the Voigtian profile A_{Voigt} specified by the widths of the Lorentzian and Gaussian components, γ_L and γ_G, is immediately given by

$$A_{\text{Voigt}} = 2\pi\gamma_L. \qquad (39)$$

The integral breadth B_{Voight} of the Voigtian profile is exactly given by

$$B_{\text{Voigt}}^{-1} = \int_{-\infty}^{\infty} F_L(\xi; \gamma_L)F_G(\xi; \gamma_G)\,d\xi$$
$$= (1/\pi^{1/2}\gamma_G)\exp(\gamma_L^2/\gamma_G^2)\,\text{erfc}(\gamma_L/\gamma_G), \qquad (40)$$

where $\text{erfc}(x)$ is the complementary error function defined by

$$\text{erfc}(x) = (2/\pi^{1/2})\int_{x}^{\infty}\exp(-t^2)\,dt. \qquad (41)$$

When the crystallites have spherical shape, the area-weighted average diameter $\langle D \rangle_A \equiv \langle D^3 \rangle/\langle D^2 \rangle$ is related to the Fourier initial slope of the peak profile on the d^* scale by

$$\langle D \rangle_A = (3/2)A_{\text{Voigt}}^{-1}, \qquad (42)$$

and the volume-weighted average diameter $\langle D \rangle_V \equiv \langle D^4 \rangle/\langle D^3 \rangle$ is related to the integral breadth as follows (Ida, Shimazaki et al., 2003):

$$\langle D \rangle_V = (4/3)B_{\text{Voigt}}^{-1}. \qquad (43)$$

APPENDIX B
Modification of the March–Dollase correction for asymmetric reflection

The pole-figure profile of the March–Dollase model (Dollase, 1986) is given by

$$p(\alpha) = (2\pi)^{-1}(r^2\cos^2\alpha + r^{-1}\sin^2\alpha)^{-3/2}. \qquad (44)$$

Since the scattering vector is parallel to the face normal direction in flat-plate symmetric reflection measurements, the preferred-orientation factor for a given reciprocal-lattice vector at the angle α from the axis of symmetry is equivalent to the pole-figure profile.

However, the direction of the scattering vector is generally deviated by $\gamma \equiv |\Theta_i - \theta|$ from the face normal in asymmetric reflection measurements, where Θ_i is the incident glancing angle and θ is the Bragg angle. Therefore, the preferred-orientation factor should be evaluated by

$$P(\alpha, \gamma) = \int_0^{2\pi} p[\arccos(\sin\alpha\sin\gamma\cos\varphi + \cos\alpha\cos\gamma)]\,d\varphi$$
$$= \pi^{-1}\int_0^{\pi}[r^{-1} + (r^2 - r^{-1})(\sin\alpha\sin\gamma\cos\varphi$$
$$+ \cos\alpha\cos\gamma)^2]^{-3/2}\,d\varphi. \qquad (45)$$

References

Albertsson, J. & Abrahams, S. C. (1989). *Acta Cryst.* B**45**, 34–40.
Abrahams, S. C. & Bernstein, J. L. (1969). *Acta Cryst* B**25**, 1233–1236.
Dollase, W. A. (1986). *J. Appl. Cryst.* **19**, 267–272.
Hart, M., Cernik, R. J., Parrish, W. & Toraya, H. (1990). *J. Appl. Cryst.* **23**, 286–291.
Ida, T. (2005). *J. Appl. Cryst.* **38**, 795–803.
Ida, T., Ando, M. & Toraya, H. (2000). *J. Appl. Cryst.* **33**, 1311–1316.
Ida, T., Hibino, H. & Toraya, H. (2001). *J. Appl. Cryst.* **34**, 144–151.
Ida, T., Hibino, H. & Toraya, H. (2003). *J. Appl. Cryst.* **36**, 181–187.
Ida, T. & Iwata, Y. (2005). *J. Appl. Cryst.* **38**, 426–432.
Ida, T., Shimazaki, S., Hibino, H. & Toraya, H. (2003). *J. Appl. Cryst.* **36**, 1107–1115.
Ida, T. & Toraya, H. (2002). *J. Appl. Cryst.* **35**, 58–68.
Poppe, G. P. M. & Wijers, C. M. J. (1990). *ACM Trans. Math. Software*, **16**, 38–46.
Stepanov, S. A. (2005). *X-ray Dynamical Diffraction Data on the Web*, http://sergey.gmca.aps.anl.gov/x0h.html.
Toraya, H., Hibino, H. & Ohsumi, K. (1996). *J. Synchrotron Rad.* **3**, 75–83.
Toraya, H., Huang, T. C. & Wu, Y. (1993). *J. Appl. Cryst.* **26**, 774–777.
Williamson, G. K. & Hall, W. H. (1953). *Acta Metall.* **1**, 22–31.